JGR Atmospheres

RESEARCH ARTICLE
10.1029/2023JD040145

High-Resolution Climate Simulations Over the Eastern Mediterranean Black Sea Region Using the Pseudo-Global Warming Method With a CMIP6 Ensemble

S. Çağatay Bağçaci[1,2], Ismail Yücel[2], M. Tugrul Yilmaz[2], Omer L. Sen[3], and Patrick Ludwig[4]

[1]Civil Engineering Department, Karamanoglu Mehmetbey University, Karaman, Türkiye, [2]Civil Engineering Department, Middle East Technical University, Ankara, Türkiye, [3]Eurasia Institute of Earth Sciences, Istanbul Technical University, Istanbul, Türkiye, [4]Institute of Meteorology and Climate Research, Karlsruhe Institute of Technology, Karlsruhe, Germany

Key Points:

- The WRF-PGW simulations perfectly capture the low-level circulation change and warming/drying signals from CMIP6 for the EMBS in winter
- The WRF-PGW simulations show heat-low formation over the EMBS in summer, in line with the CMIP6 GCM ensemble
- The new insights appear in future summer precipitation increases over the Greater Caucasus and nearby regions

Supporting Information:

Supporting Information may be found in the online version of this article.

Correspondence to:

S. Ç. Bağçaci,
scbagcaci@kmu.edu.tr

Citation:

Bağçaci, S. Ç., Yücel, I., Yilmaz, M. T., Sen, O. L., & Ludwig, P. (2024). High-resolution climate simulations over the Eastern Mediterranean Black Sea region using the pseudo-global warming method with a CMIP6 ensemble. *Journal of Geophysical Research: Atmospheres*, *129*, e2023JD040145. https://doi.org/10.1029/2023JD040145

Received 11 OCT 2023
Accepted 4 MAY 2024

Author Contributions:

Conceptualization: S. Çağatay Bağçaci, Ismail Yücel
Data curation: S. Çağatay Bağçaci
Formal analysis: S. Çağatay Bağçaci
Funding acquisition: M. Tugrul Yilmaz
Investigation: S. Çağatay Bağçaci
Methodology: S. Çağatay Bağçaci, Ismail Yücel
Software: S. Çağatay Bağçaci
Supervision: Ismail Yücel, M. Tugrul Yilmaz
Validation: S. Çağatay Bağçaci
Visualization: S. Çağatay Bağçaci
Writing – original draft: S. Çağatay Bağçaci

Abstract The strong drying expected in the Eastern Mediterranean with climate change could cause mass migration of people already living under water shortages. On the other hand, precipitation is expected to increase toward the region's north, particularly those along the interior of the eastern Black Sea coasts, which could worsen existing floods. However, this double-sided adverse phenomenon and its underlying reasons have been investigated by relatively low-resolution models in the Eastern Mediterranean Black Sea (EMBS) region, where orographic precipitation prevails. This study performs 4 km resolution Weather Research and Forecasting (WRF) model simulations with and without climate change signals retrieved from a CMIP6 GCM ensemble via pseudo-global-warming (PGW). The WRF simulations captured the large-scale dynamics affecting the EMBS fairly well: an anticyclonic low-level circulation and enhancing subsidence stem from anomalous ridge development over the central Mediterranean in winter (DJF), and a cyclonic low-level circulation and weakening subsidence rise from heat-low development over the Eastern Mediterranean in summer (JJA). The resulting picture of future warming and drying over the area generally supports the literature, although new insights emerge in anomalous precipitation increase, especially in the summer season over the Greater Caucasus and nearby regions. Most likely, the warmer-than-expected Caspian Sea induces a large increase in specific humidity and, thus, a large moisture source in the lower troposphere and an extension of the heat-low effect in the mid-troposphere. In addition, the high-resolution WRF simulations provide added value over the complex topography of the Caucasian Mountain range for new insights into this region.

Plain Language Summary One of the most vulnerable parts of the Mediterranean climate change hotspot is the Eastern Mediterranean Black Sea (EMBS) region. The future climate change signal of the state-of-the-art CMIP6 GCM ensemble between 2071–2100 and 1985–2014 periods was retrieved for the region under the Shared Socioeconomic Pathway (SSP5-8.5). The signal was used to perturb ERA5 reanalysis data for the IPCC AR6 baseline period, 1995–2014, in the context of the pseudo-global warming (PGW) method. The Weather Research and Forecasting (WRF) model was used to obtain very high-resolution (4 km) climate data. According to the study, the future winters were as expected: anomalous ridge formation over southern Italy, resultant northeasterlies over the EMBS, the large-scale mid- and upper tropospheric subsidence, attenuation of the land-sea temperature contrast and finally, strong drying. The summers exhibit negative vertical pressure velocity changes, strengthening Etesians, and strong surface warming in line with the expectations of the literature. However, summers brought anomalous precipitation to the Greater Caucasus and nearby areas in our high-resolution WRF simulations. We think these new insights are primarily caused by the warmer-than-expected Caspian Sea stemming from the SST availability among the ensemble, a very convective environment for the region and better-resolved complex-orography-induced precipitation.

1. Introduction

The Mediterranean climate prevails between the arid subtropics of Africa and mild midlatitudes of Europe, characterized by dry summers with warm to hot temperatures and mild but wet winters. The Mediterranean region, however, spans a vast area, encompassing diverse climatic conditions alongside geographical features, such as peninsulas, steep orography, gulfs, and islands of various sizes. Located between the Mediterranean, Aegean, and Black Seas, the Anatolian Peninsula (AP) and its surrounding regions represent a climatic transition zone referred to as the Eastern Mediterranean Black Sea region (EMBS; here defined between 22–53°E and 33–45°N

Writing – review & editing:
Ismail Yücel, M. Tugrul Yilmaz, Omer L. Sen, Patrick Ludwig

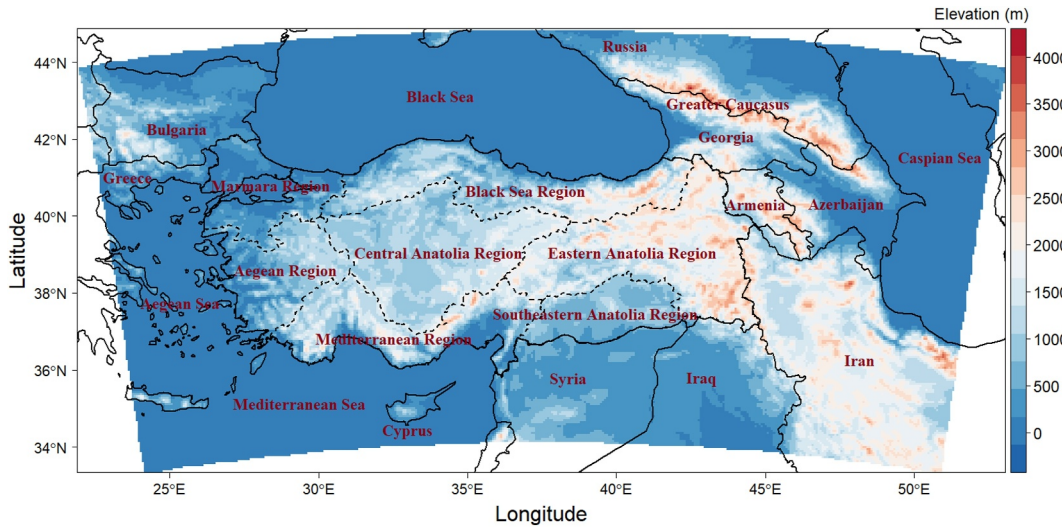

Figure 1. The study area elevation map. The solid line divides the borders of countries, and the dashed line divides the borders of seven geographical regions of Türkiye.

as shown in Figure 1). The Mediterranean and Aegean coasts have a typical Mediterranean climate, while the midland AP has a semi-arid continental environment with hot, dry summers and cold, snowy winters. On the other hand, the Black Sea coasts and the Greater Caucasus to the northeast receive continuous rainfall throughout the year. Subarctic climate prevails under the Siberian high in the east of the AP, and high mountain ranges cause prolonged cold winters and short, cool summers.

Due to its expected high response to the increased radiative forcing associated with greenhouse gas (GHG) emission scenarios, the Mediterranean region is one of the leading hotspots of climate change (Giorgi, 2006). A sharp decrease in mean precipitation and an increase in variability (tending to show more extremes) combined with rising temperatures make the region vulnerable to natural disasters, such as floods, droughts, desertification, and wildfires. Intergovernmental Panel on Climate Change Assessment Report 6 (IPCC AR6, 2021) and some recent studies have shown that the southern and western parts of the EMBS region are among the most seriously affected areas of this hotspot (Barcikowska et al., 2018, 2020; Önol et al., 2014; Tuel & Eltahir, 2020). The cold season precipitation decrease in this hotspot region is more than 10% at 3°C warmer world relative to 1995–2014 under the SSP5-8.5 scenario (Ali et al., 2022). The region is densely populated, and people rely on limited water resources for domestic use, agriculture, and industry. On the other hand, the northeastern part of the EMBS has high annual precipitation totals and an expected increase in the amount and extremes may exacerbate existing flood risks (Bağçaci et al., 2021). In the east, the effects of climate change that are already being felt are expected to alter the timing of snowmelt runoff in the Euphrates–Tigris basin, which has two main snow-fed transboundary rivers that supply water to southeastern Türkiye, Syria, and Iraq (Sen et al., 2011; Yucel et al., 2015). An increase in temperature and a decrease in precipitation over the upstream highlands have caused a reduction in snow cover area and snow water equivalent, leading to earlier snowmelt and a reduction in annual runoff (Bozkurt & Sen, 2013; Yucel et al., 2015), which is vital for the water-stressed people living already in civil war conditions like in Syria (Tuel & Eltahir, 2020). These facts make the current and future climate of the EMBS vitally important and require detailed investigations based on state-of-the-art global climate models (GCMs) and subsequent dynamically downscaled, high-resolution projections.

The summer (JJA) climate over the EMBS is mainly driven by the stabilizing effect of cold air advection by steady, low-level northerly flow, that is, the Etesians and adiabatic warming of mid and upper tropospheric subsidence winds (Barcikowska et al., 2020; Poupkou et al., 2011; Tyrlis & Lelieveld, 2013; Ziv et al., 2004). The first is characterized by the large-scale sea-level pressure (SLP) dipole between the Middle East and central and southeastern Europe (Anagnostopoulou et al., 2014). The resulting low-level circulations intersect over the Aegean Sea with the funnel effect and are strengthened by mid and upper-tropospheric subsidence (Barcikowska et al., 2020; Rodwell & Hoskins, 2001). The latter is part of the Indian summer monsoon desert mechanism (Barcikowska et al., 2020; Rodwell & Hoskins, 1996), suppressing precipitation with a strong ridge over the

western EMBS, including most of the Anatolian plateau. However, northeastern Anatolia and the Greater Caucasus and their Black Sea coasts (in the northeastern EMBS) are located in a buffer zone of subsidence with a weak ascent at the mid (500 hPa) tropospheric level (Simpson et al., 2015). In contrast to the typical Mediterranean climate, these regions are rainy all year round and have low seasonality. Barcikowska et al. (2020) investigated the effect of summer season surface warming on the local circulation over the area encompassing the EMBS region by comparing the 300 warmest and coolest summers (July). The authors showed that surface warming leads to mid-tropospheric subsidence over northeastern Anatolia and the Greater Caucasus, which wipes out the buffer zone proposed by Simpson et al. (2015). According to the authors, surface warming is also leading to enhanced heat-low conditions over the Eastern Mediterranean and Arabian Peninsula. Meanwhile, enhanced SLP over the Balkans and the Black Sea suppresses relative humidity and precipitation over those regions. However, they did not focus on sea surface temperature (SST). They also employed a relatively low-resolution GCM (GFDL CM2.5 with approximately 50 km horizontal resolution), which is limiting to gaining comprehensive insights into the complex terrain-induced precipitation over the regions mentioned above. In addition, the authors underline that surface warming overcomes the counterbalancing effects of the Etesians and the summer North Atlantic Oscillation (SNAO) over the EMBS. Therefore, further investigations with fine-scale regional climate models (RCMs) are necessary to gain more insights into how the local circulation of the EMBS region responds to the thermal-originating "dipole-like" formation mentioned above.

In winter (DJF) or the wet season (NDJFM), the North Atlantic Oscillation (NAO), El Niño/Southern Oscillation (ENSO), Eastern Atlantic-Western Russia (EA/WR) teleconnections, and a remote link between East Asian and Mediterranean troughs affect the climate conditions of the EMBS (Alpert et al., 2006; Duzenli et al., 2018; Kadioğlu et al., 1999; Kutiel & Benaroch, 2002; Sen et al., 2019; Trigo et al., 2006; Tuel & Eltahir, 2020; Xoplaki, 2002). The NAO is the most studied and well-documented mode of variability for the Mediterranean winter climate. It determines the direction and strength of the prevailing wind patterns over the EMBS. An increased Iceland pressure pattern leads to the southwesterlies that moisten the western and southern parts of the region with ascending warm and humid air (Eshel & Farrell, 2000; Türkeş & Erlat, 2006; Xoplaki et al., 2004). A decreased Iceland pressure pattern (positive NAO) makes the region drier with the northeasterlies and descending cold and dry air. By the end of the 21st century, in a changing climate, a more positive NAO phase and a weakening of the Mediterranean storm track are expected under the SSP3-7.0 and SSP5-8.5 scenarios (IPCC AR6, 2021). On the other hand, the Mediterranean is one of the rare areas where an anomalous ridge can develop with respect to climate change and affect a landmass that is inhabited by humans (Tuel & Eltahir, 2020). These factors cause significant precipitation decline over the Mediterranean, opposite the general precipitation increase expectations around most regions on Earth. As well as other main driving factors, that is, high tropical amplification and enhancing stratospheric vortex (Zappa & Shepherd, 2017) and reduction in the low-level (850-hPa) equator-to-pole air temperature gradient in the Northern Hemisphere (Catto et al., 2019), the anomalous ridge development is expected to suppress cyclogenesis over the EMBS region, which hosts one of the three most cyclone-active seas in the Mediterranean, that is, the Aegean Sea (Lionello et al., 2006; Trigo et al., 2002; Tuel & Eltahir, 2020). On the other hand, the changing patterns mentioned above do not seem to reduce the precipitation in the northern and northeastern EMBS, including another cyclone-active sea, the Black Sea, but somewhat further increase heavy precipitation (Barcikowska et al., 2018; Lionello et al., 2006; Şen et al., 2015; Trigo et al., 2002). Here, the frequent cyclones are triggered by vorticity advection from a westerly positioned upper trough (Mastrantonas et al., 2021). The prevailing wind patterns favor the upslope lifting toward the region's steep orography (Önol, 2012). However, Tuel and Eltahir (2020) have shown that attenuation of the land-sea temperature contrast, as an independent component, may produce an anticyclone and suppress precipitation over the EMBS, including its northern and northeastern parts in winter. According to IPCC AR6 (2021), the northern and northeastern EMBS regions are expected to experience precipitation increases under different warming levels based on the EURO-CORDEX RCM simulations (40 models), which were driven by GCM outputs from the Coupled Model Intercomparison Project (CMIP) phase 5 experiment under the RCP8.5 scenario. Thus, attenuation of land-sea temperature contrast seems unable to suppress precipitation over the region. This picture needs to be further assessed by high-resolution CMIP6-forced RCM simulations under an equivalent scenario, the SSP5-8.5.

GCMs are the most relevant tools to create climate change projections in the context of the CMIP phases. The quantification of GHGs concentrations has been updated with the latest phase of CMIP, CMIP6 (Bağçaci et al., 2021; Eyring et al., 2016). The utilization of CMIP6 GCMs in Mediterranean climate change studies is

crucial since the region is notably sensitive to increasing GHGs concentrations (Tuel & Eltahir, 2020). As the CMIP6 GCMs have a rather coarse resolution (~50–500 km), they need to be further dynamically downscaled by RCMs to obtain more reliable regional information. To the best of our knowledge, no dynamical downscaling study involving CMIP6 projections has been conducted for the EMBS region. Before dynamical downscaling, the GCMs uncertainties appertaining to model parameterization and unprescribed forcings should be considered (Ahmed et al., 2019; Bağçaci et al., 2021; Kim et al., 2016; Li et al., 2019). Using a multi-model ensemble (MME) of GCMs is a common approach in climate change-related studies to overcome these uncertainties. Likewise, RCM MMEs should be considered because the uncertainties and biases of GCMs propagate into the RCMs via the boundary conditions (Dutheil et al., 2020). However, the dynamic downscaling of GCMs individually is computationally expensive and certainly needs bias correction of user-relevant output variables. As an alternative, the pseudo-global warming (PGW) approach, introduced by Schär et al. (1996), is increasingly used to overcome those issues (Dutheil et al., 2020; Fujihara et al., 2008; Hunt et al., 2020; Ikeda et al., 2021; Li et al., 2019; Liu et al., 2017; Zhang et al., 2016). In this method, historical gridded reanalysis data are perturbed by the climate change signal, the difference between future and historical mean climate conditions, retrieved from the MME of GCMs (Li et al., 2019; Liu et al., 2017). Therefore, uncertainties are considered within the range of MME. In this study, we will provide very high-resolution (4 km horizontal grid spacing) simulations of the current and future climates for the EMBS based on the dynamical downscaling of a CMIP6 GCMs ensemble via the PGW method. The content of this study is summarized below:

Section 2 describes the model and numerical experiments used in the study and the data for the model verification. In the first part of Section 3, the validation of the simulations for current climate conditions with ground and gridded observation data sets is presented. The second part focuses on future seasonal precipitation changes based on both the GCM ensemble and the RCM simulations. The third part of Section 3 describes the "dynamic" and "thermodynamical" factors controlling the seasonal precipitation changes. The last part of Section 3 is allocated to additional analysis related to available SST warming differences to explain the anomalous precipitation increase over the Greater Caucasus and nearby regions, particularly during the summer season. Section 4 discusses the results, and Section 5 concludes this study.

2. Regional Climate Model (RCM) Setup and Numerical Experiments

2.1. RCM Setup and Study Area

The Weather Research and Forecasting (WRF) model Version 4.3 (Skamarock et al., 2021) was used as the RCM for the dynamical downscaling simulations presented in this study. The WRF simulations were performed with the GHG concentrations retrieved from the fossil-based economic development scenario of CMIP6 Shared Socioeconomic Pathway (SSP5-8.5), which predicts 8.5 Wm^{-2} radiative forcing in 2100. The WRF model covers the EMBS domain, as shown in Figure 1. The domain has 625 × 300 grid points with 4 km horizontal grid spacing. The model time step for integration is 24 s. The domain extends 2,500 km in the west-east and 1,200 km in the south-north direction. Forty vertical levels were used up to a height of 50 hPa. We performed spectral nudging, first introduced by Waldron et al. (1996) and further developed by Von Storch et al. (2000) for applications in RCMs, to retain the coherence of the large-scale forcing in the dynamical downscaling simulations. Miguez-Macho et al. (2004) adapted spectral nudging to the Regional Atmospheric Modeling System (RAMS), and later, they implemented the technique in the WRF-ARW in 2010 (Skamarock et al., 2021). We used a wavelength of 1,250 km in the zonal direction and 1,200 km in the meridional direction. These wavelengths nearly represent the division between synoptic and convective scale flows (Gómez & Miguez-Macho, 2017) and are shown to be optimal in simulating precipitation and near-surface variables (Gómez & Miguez-Macho, 2017; Huang et al., 2021; Wang & Kotamarthi, 2013). We utilized relatively weak nudging coefficients (0.0003 s^{-1}, roughly corresponds to the 1hr e-folding time) to avoid interfering significantly with the model's ability to evolve freely in the mesoscale. Depending on the height above Planetary Boundary Layer (PBL), nudging starts roughly at 1,500 m above the terrain (no nudging was applied inside the PBL), and its strength increases smoothly until it becomes constant in the upper troposphere (Miguez-Macho et al., 2004, 2005). We nudged the geopotential, temperature and horizontal wind components as Liu et al. (2017) did in their PGW-based study conducted over North America. The general convention of the nudging strategy is given by Equation 1 (adapted from Van Garderen et al. (2021)) as below:

Table 1
Ensemble Members, Variant Label (Ens. Used), and Horizontal Resolutions of CMIP6 GCMs Used in the Ensemble

CMIP6 GCM	Ens. used	Resolution (x, y)
AWI-CM-1-1-MR	r1i1p1f1	0.94 × 0.94
BCC-CSM2-MR	r1i1p1f1	1.10 × 1.10
CMCC-CM2-SR5*	r1i1p1f1	1.25 × 0.94
CMCC-ESM2*	r1i1p1f1	1.25 × 0.94
CNRM-CM6-1-HR	r1i1p1f2	0.50 × 0.50
EC-Earth3	r1i1p1f1	0.70 × 0.70
EC-Earth3-CC	r1i1p1f1	0.70 × 0.70
EC-Earth3-Veg	r1i1p1f1	0.70 × 0.70
FGOALS-f3-L	r1i1p1f1	1.25 × 1.00
GFDL-ESM4	r1i1p1f1	1.30 × 1.00
HadGEM3-GC31-MM*	r1i1p1f3	0.80 × 0.60
MPI-ESM1-2-HR	r1i1p1f1	0.90 × 0.90
MRI-ESM2-0	r1i1p1f1	1.13 × 1.12

Note. GCMs giving SST information for the Caspian Sea were shown with an asterisk.

$$\frac{\partial X}{\partial t} = \begin{cases} F_X + G(X_{\text{ERA5,perturbed ERA5}} - X) & \text{above PBL} \\ F_X & \text{otherwise} \end{cases} \quad (1)$$

where X is the variable to be nudged (geopotential, temperature or horizontal wind components), F_x is the model tendency for variable X, and X_{ERA5} and $X_{\text{perturbed ERA5}}$ are the state of that variable in ERA5 and its perturbed version, respectively. The vertical threshold is the height of the PBL, namely, no nudging is applied in the boundary layer. G is the relaxation coefficient in units of s^{-1}, determining the nudging strength. Nudging is performed at every time step.

The parameterization schemes used in this study are the new Thompson microphysics scheme (Thompson et al., 2008), the Yonsei University (YSU) PBL scheme (Hong et al., 2006), the Rapid Radiative Transfer Model (RRTMG) (Iacono et al., 2008), and the Noah land surface model (Chen & Dudhia, 2001). We used the cumulus parameterization Tiedtke scheme (Tiedtke, 1989; Zhang et al., 2011) as this option yielded better precipitation results than convection-permitting simulations in 4 km for the Türkiye domain. This result was obtained in the sensitivity tests conducted with the 60-combination of model physics for 2020 (Bağçacı, 2023).

2.2. Numerical Experiments

Two 20-year WRF simulations for dynamic downscaling of ERA5 were performed for the IPCC AR6 baseline period, 1995–2014, as a retrospective and its corresponding future period. The corresponding future period was obtained by adding GCM ensemble delta change between 2071–2100 and 1985–2014 to ERA5 in the baseline period, which is more detailed below. The model was started 1 year before the baseline period, that is, 1994, for the model spin-up, which was not used in later analysis. In the first experiment, the model was forced with the 6-hourly ∼0.25° ERA5 reanalysis data, including 6-hourly SST updates, to obtain hindcast simulations over the targeted domain at 4 km resolution. Liu et al. (2017) used a one-way nesting WRF setup to dynamically downscale ∼0.7° ERA-Interim data to 4 km without needing any intermediate coarse resolution nesting option. Similarly, we did not use any inner coarse resolution nesting option in the dynamical downscaling of ERA5 reanalysis and its perturbed version.

The second experiment is based on the perturbation of the ERA5 reanalysis data by the climate change signal derived from 13 CMIP6 GCMs run with the SSP5-8.5 emission scenario (Table 1) to obtain the pseudo-future projections. These 13 GCMs were selected according to their performances (Bağçaci et al., 2021) and relatively high resolution. We have only selected GCMs not exceeding four times the spatial resolution of ERA5 to alleviate information loss in the bilinear interpolation. Only three GCMs out of the full ensemble give SST information for the Caspian Sea. This issue is discussed later in the "Impact of SST availability in the GCM ensemble" section to justify the anomalous precipitation increase over the Greater Caucasus and nearby regions.

The 20-year (January 1995–December 2014) simulation was forced with 6-hr ERA5 reanalysis plus a delta for the climate change signal:

$$\text{PGW}_{\text{forcing}} = \text{ERA5} + \Delta\text{CMIP6}_{\text{SSP585-historical}} \quad (2)$$

where $\Delta\text{CMIP6}_{\text{SSP585-historical}}$ is the 30-year CMIP6 MME mean monthly differences:

$$\Delta\text{CMIP6}_{\text{SSP585-historical}} = \text{CMIP6}_{2071-2100} - \text{CMIP6}_{1985-2014} \quad (3)$$

The procedure of the PGW methodology, developed by Schär et al. (1996), is explained in more detail in Figure 2. The first step combines the two equations (Equations 2 and 3) described above. Initially, the vertical (linear) and horizontal (bilinear) interpolation was performed to equate the vertical and horizontal resolution of GCMs to those of ERA5, respectively. Afterward, monthly means were calculated for the historical (1985–2014) and future

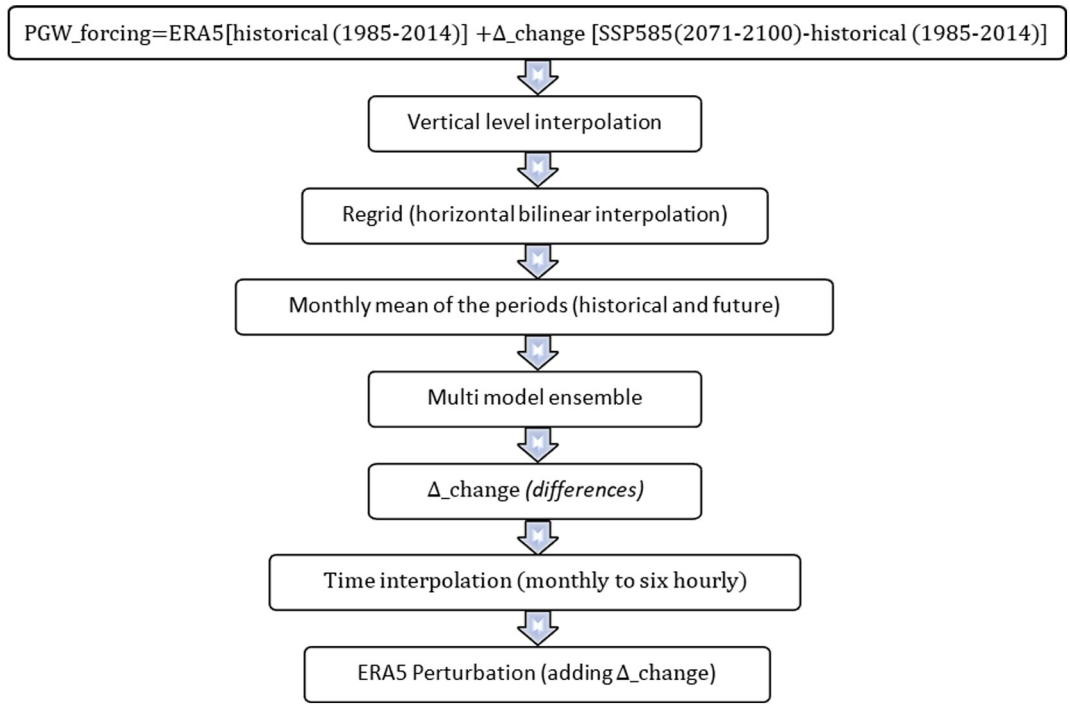

Figure 2. The PGW methodology flowchart.

(2071–2100) periods and MMEs were constructed. Then, the difference between future and historical period MMEs (Δ_change) was interpolated to 6-hourly periods (temporal interpolation). In the last step, these time-interpolated deltas were added to ERA5 (perturbation) both for surface and pressure levels to construct the PGW-forcing data set. The perturbed variables are given in Table 2.

2.3. Model Verification and Data

We have used ground observations and three gridded data sets to verify precipitation, and the ground observations and two gridded data sets to verify near-surface temperature results of the WRF retrospective simulation. The ground observations were retrieved from Türkiye's General Directorate of Meteorology (GDM) for the territory of Türkiye, covering a considerable amount of the land surface within the study area. The ground station-based observations, used as a validation data set for precipitation, include 273 stations providing daily and 614 stations for monthly data. For the validation of near-surface temperature, the stations used are 417 and 1506, respectively. Besides, 119 station data records retrieved from the World Meteorological Organization (WMO) were used for near-surface temperature validation for the regions outside Türkiye. In order to keep the written text concise,

Table 2
Data Fields in the PGW Perturbation to Force WRF

Surface level	Near-surface relative humidity	Pressure level	Relative humidity
	Near-surface temperature		
	U10 (eastward wind)		Eastward wind
	V10 (northward wind)		
	Sea-level pressure		Northward wind
	Surface pressure		
	Skin temperature		Air temperature
	Sea-surface temperature		
	Soil temperature		Geopotential height

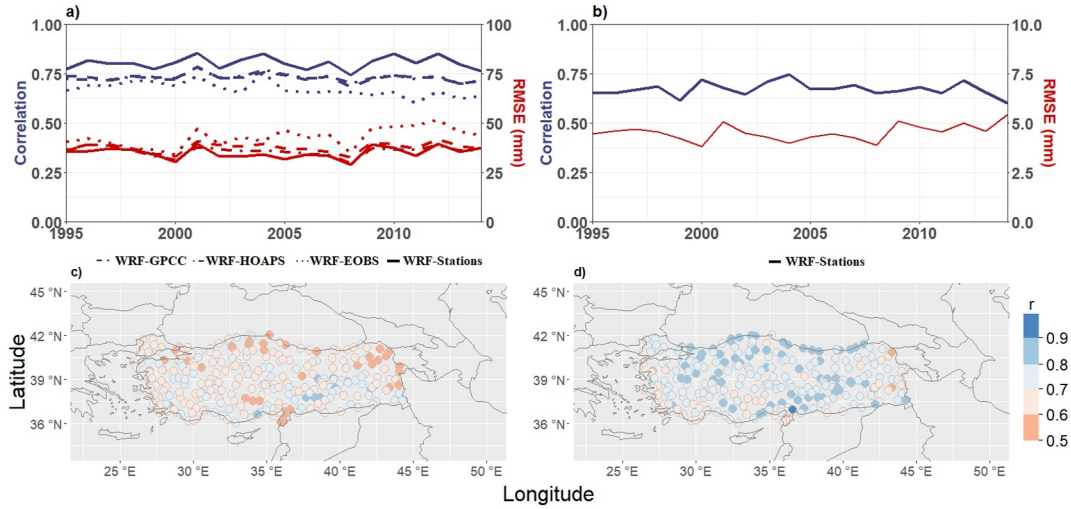

Figure 3. The WRF simulations precipitation statistics between 1995–2014: (a) the monthly precipitation correlation (the left axis with the blue lines) and RMSE (the right axis with the red lines). The solid line denotes the WRF-ground observation statistics, the dashed line denotes the WRF-GPCC statistics, the dot-dashed line denotes the WRF-GPCC HOAPS statistics, and the dotted line denotes the WRF-EOBS statistics. (b) As in a, but for daily precipitation statistics between WRF and ground observations. (c) The spatial distribution of daily precipitation correlations between WRF and ground observations for the 1995–2014 period over Türkiye. (d) As in (c), but for the wet season (NDJFM).

ground station-based observations (i.e., both precipitation and near-surface temperature) will henceforth be referred to as "Station" in this study.

We also used the Global Precipitation Climatology Centre (GPCC, Schneider et al., 2022) monthly precipitation data set at 0.25° resolution, HOAPS/GPCC (Schröder et al., 2019) global daily precipitation data record at 0.5° resolution, EOBS (Cornes et al., 2018) daily precipitation and the near-surface temperature product at 0.1° resolution, and the Climate Research Unit at the University of East Anglia (CRU version 3.22, 1901–2013; Harris et al. (2014)) monthly near-surface temperature product at 0.5° resolution. The gridded observation data sets cover the entire EMBS domain except for EOBS, which ends at 45° E. Nevertheless, EOBS provides gridded observations over most of the domain. We use the monthly mean of the gridded daily precipitation for validation since the definitions for the 24-hr precipitation sums may differ (midnight to midnight or morning to morning measurements) across the countries (ECMWF, 2020).

3. Results

3.1. Validation

Correlations and RMSE statistics between monthly precipitation values of WRF and four reference products (EOBS, GPCC, GPCC-HOAPS, and Station) were calculated. Figure A1 in Supporting Information S1 provides seasonal mean precipitation of the historical WRF simulations for 1995–2014. The WRF simulations were regridded to each of the gridded data products' native resolution. The WRF-Station statistics were calculated by the nearest neighbor points of the WRF grids to Station locations. Overall, correlations between WRF and EOBS vary between 0.60 and 0.76 and are consistently lower than other pairs (i.e., WRF-GPCC, WRF-HOAPS, WRF-Station) for the 1995–2014 period (Figure 3a). The monthly RMSE values are between 34 and 52 mm for WRF-EOBS, which are consistently higher than the WRF-other product comparisons. When GPCC-HOAPS is used as the reference, WRF produces slightly better results (i.e., correlation and RMSE) than GPCC, where both correlation values range between 0.70 and 0.79. The monthly RMSE values against GPCC-HOAPS are marginally (3 mm) lower than those against GPCC and fall between 29.8 and 39.2 mm. The RMSE values between WRF and Station vary between 29.1 and 39.7 mm, while the correlations range from 0.74 to 0.86; on average, WRF correlations against Station are higher than against other reference products (GPCC and GPCC-HOAPS), while RMSE values are quite similar. The spatial distributions of monthly precipitation correlations between WRF and gridded reference data products for 1995–2014 are shown in Figure A2 of the Supporting Information S1.

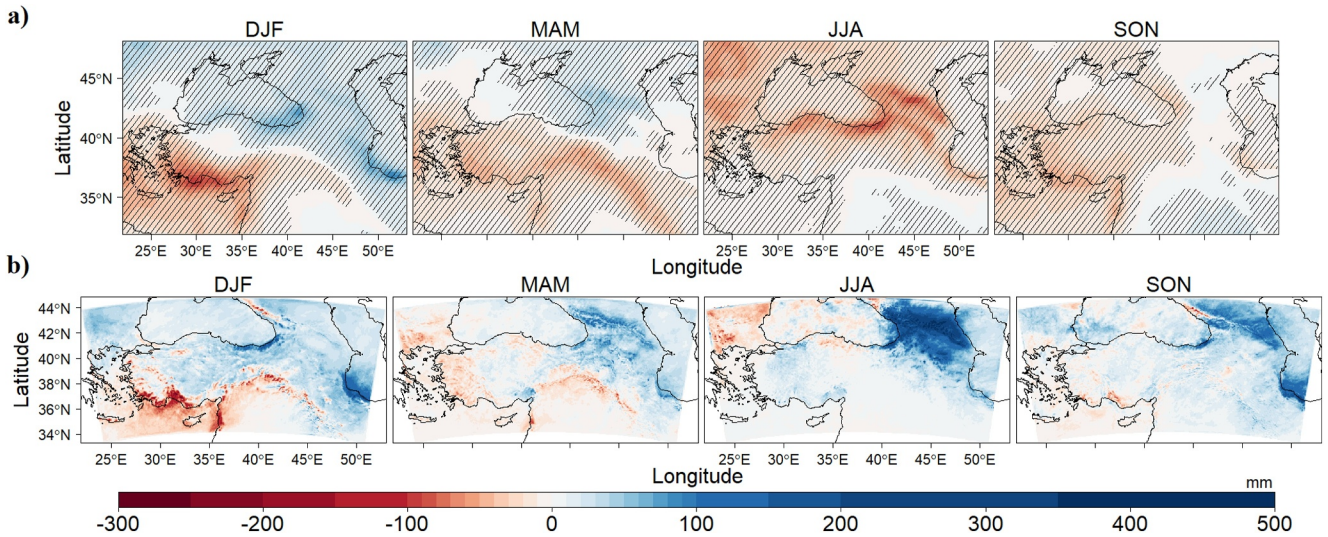

Figure 4. Seasonal precipitation changes (a) between 2071–2100 and 1985–2014 retrieved from 13 CMIP6 GCM models ensemble. The statistically significant changes at $p \leq 0.05$ level are hatched. (b) Between 1995–2014 and the corresponding pseudo-future period obtained from the 4-km WRF simulations over the EMBS domain.

Given that WRF precipitation statistics against Station are better than against other reference products (Figure 3a), from now on, only Station-based daily statistics are shown (Figure 3b) for the validation period. The daily correlation values vary between 0.60 and 0.75, and the RMSE values range between 3.8 and 5.4 mm. The spatial distributions of daily correlations between WRF- and Station-based precipitation are shown in Figure 3c (annual) and Figure 3d (only wet season NDJFM). The daily correlations over all stations are above 0.5 and are higher (up to 0.83) over southeastern Türkiye. The correlations over the Aegean coasts and the northwestern country (between 0.6 and 0.7) are higher than those over the easternmost Mediterranean coast and the northeastern regions (between 0.5 and 0.6). Except for these areas, the spatial variability of the correlations is low. The wet season daily correlations are in better agreement than the correlations calculated using the whole year (Figure 3d). The daily correlations for the wet season are between 0.7 and 0.9 for most of the country, while the Aegean coasts and some parts of the Mediterranean coasts show slightly lower correlations between 0.6 and 0.7.

The near-surface temperature correlations are by far better between WRF and the reference data sets than the precipitation-based correlations (Figure A3 in Supporting Information S1). Daily temperature correlations between WRF and the reference products EOBS and Station are 0.97 and 0.98, where the RMSE values are 2.53 and 1.78°C, respectively. On the other hand, the monthly temperature correlations between WRF and reference products CRU and Station are 0.97 and 0.99, where the RMSE values are 2.37 and 1.48°C, respectively. It should be noted that we did not apply a high-pass filter. The correlations were computed throughout the reference period (1995–2014) for each day (daily correlation) or month (monthly correlation) as a whole where the observations exist.

3.2. Seasonal Future Precipitation Change

Considering future changes, the GCM MME shows a substantial precipitation decrease of up to 100 mm over the Mediterranean and Aegean coasts of the EMBS region in winter; such drier conditions are projected to reach the inner Anatolian Peninsula (AP) in the north and Cyprus, Crete, and Syrian Mediterranean coasts in the south, with a gradual decline down to 35–40 mm (Figure 4a). A similar pattern can be observed over the north of the Fertile Crescent with decreasing amounts around 15 mm. On the other hand, the GCM MME projects an increase in precipitation of up to 80 mm over the southeast coasts of the Black Sea and southwest coasts of the Caspian Sea. The precipitation increase is around 25–35 mm over the inner domains between these regions, including Greater Caucasus and northeastern Anatolia. The decreases/increases are statistically significant at a 95% confidence interval (throughout the study, statistically significant changes are presented with the *t*-test at $p = 0.05$ level). The high-resolution WRF simulation captures the pattern at a reasonable level, however, with enhanced magnitudes (Figure 4b). The decrease in winter precipitation over the Mediterranean coasts and the inner highlands of Türkiye, which receives most of the annual precipitation because of its steep topography, is almost two-and-a-

half-fold that of the GCM ensemble. Stronger precipitation reduction is also present over the pattern-like regions mentioned above. The regions with increased precipitation also cohere except for the Russian Black Sea coasts. Here, the precipitation decrease is up to 100 mm. On the other hand, the WRF simulations show a precipitation increase between 100 and 200 mm over Türkiye's northeastern Black Sea coasts, which is stronger than that of the GCM ensemble.

The spring precipitation pattern resembles winter over the southern EMBS, where the precipitation decline amount is mostly less but more widespread with both GCM MME and WRF simulations. The GCM MME and WRF simulations also have a similar pattern (but in the reverse direction, an increase) over the Greater Caucasus and northeastern Anatolia; however, with the WRF model, the increase penetrates more south along the mountainous region of eastern Anatolia. The precipitation increase is roughly between 100 and 170 mm with the WRF simulations over the Greater Caucasus, which is four times that of the GCM ensemble.

In summer, the picture becomes more different. The southeastern coasts of the Black Sea and the northwest coast of the Caspian Sea, together with the Greater Caucasus and the surrounding highlands, experience a high precipitation increase in the WRF simulations (mostly between 100 and 350 mm, and up to 500 mm for the marginal points), while the GCM ensemble expects a high statistically significant decrease of up to 90 mm (Figure 4). The southern part of the EMBS and most of the Anatolian plateau, which take far less precipitation in summer than the other seasons, also show different signs among the GCM ensemble and WRF simulations, though not as much over the Greater Caucasus and nearby regions. The GCM ensemble shows a decrease of up to 20 mm in statistically significant regions at $p \leq 0.05$ level, while the WRF simulations show an increase mostly of up to 20 mm (for the marginal points, this amount rises to 100 mm) over the region. It should be noted that precipitation increase does not exceed 2 mm over most of the Syrian and Iraqi territory with the GCM ensemble and WRF simulations. When looking at the remaining regions, the picture is more compatible. The GCM ensemble and the WRF model agree on the prominent drying and its amount over the west of the Black Sea, including northern Greece and Bulgaria, and the Black Sea coasts of the east of northernmost Anatolia when excluding marginal points.

The GCM ensemble demonstrates no statistically significant precipitation changes at $p \leq 0.05$ level over the eastern Greater Caucasus and its south, while the WRF simulations amplify precipitation over the same region in the fall season. The precipitation increase exceeds 100 mm over the Greater Caucasus and nearby regions and exceeds 200 mm over Türkiye's eastern Black Sea coast and southwest Caspian Sea coasts with the WRF simulations. The increase also penetrates toward the south and west throughout the Anatolian plateau with diminishing values. On the other hand, the drying and its amount in the southwestern Anatolian plateau, the Mediterranean and Aegean coasts of Türkiye, northern Greece, Greek islands, and Cyprus are in good agreement between the GCM ensemble and the WRF model.

3.3. "Dynamic" and "Thermodynamical" Factors

The CMIP6 GCMs, as their predecessors, that is, CMIP3 and CMIP5, show an "anomalous" ridge formation in the future over southern Italy in winter, taking effect over the whole Mediterranean (Figure 5) (Giorgi, 2006; Tuel & Eltahir, 2020). The ridge is located more northwest and loses its strength but still governs the low-level circulation over the EMBS in spring (MAM in Figure 5). In the summer season, dipole-like SLP anomaly pattern formation stands out between the Tibetan Plateau and the Eastern Mediterranean. It results in an anomalous cyclonic low-level circulation development over the EMBS. In the fall season, the anomalous low-pressure system largely diminishes over the Eastern Mediterranean; however, it still exists over North Africa and the Arabian Peninsula in the south and southern EMBS in the north (SON in Figure 5). Another anomalous low-pressure system, which may influence the circulation over the northern EMBS, is located over the eastern Caspian Sea. It also has a diminished appearance compared to summer. Overall, the spring season follows winter, and the fall season follows summer over most of the EMBS in terms of anomalous circulation patterns.

Figure 6 shows that the anomalous ridge strengthens the low-level anticyclonic circulation in winter over most of the EMBS region, from the westernmost point to the meridional line between the northwestern Greater Caucasus and the Syria-Iraq border in the east, at about 42°E. It is consistent with the GCM ensemble simulations, which show an anticyclonic response but with less intensified wind patterns (Figure A4 in Supporting Information S1). The anomalous wind flow is northwesterly and northerly in the north and northwestern EMBS, which is known to advect dry and cold air in today's climate. The advected air becomes slightly moister for the future period with a relatively small increase in specific humidity between 1 and 1.5 g/kg near the surface and about 1 g/kg in the

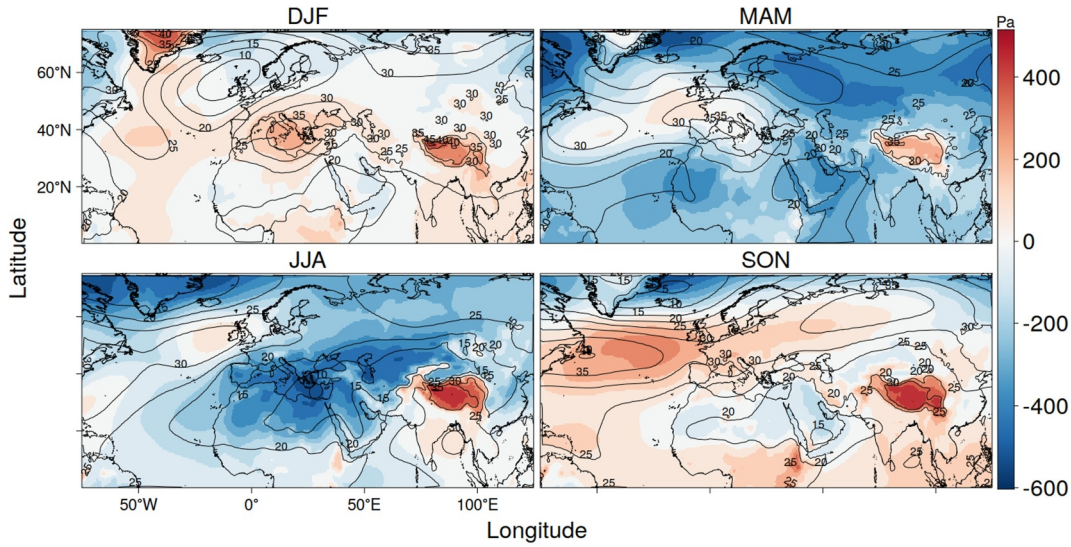

Figure 5. The large-scale 850 hPa geopotential height (contours) and SLP (shadings) change signal of the PGW forcing between 2071–2100 (future SSP5-8.5 scenario) and 1985–2014 (historical) retrieved from 13 CMIP6 GCM model ensemble. The geopotential height is in units of m, and SLP is in units of pascal.

lower troposphere (Figure 7). These factors are expected to increase precipitation over northern Bulgaria and the Black Sea Region of Türkiye by orographic enhancement, as the moistened wind patterns are perpendicular to the mountain range. This is largely the case, but the expected picture does not hold for some parts of the southwestern Black Sea Region coasts in the WRF simulations. Here, the decrease in precipitation appears to be related to mid-tropospheric subsidence (Figure 8). In the southern parts of the EMBS, precipitation decreases dramatically, consistent with the subsidence over almost all levels of the troposphere in winter. The decrease is also prominent toward the inner Anatolian Plateau from the west and the Mediterranean coast, consistent with GCM ensemble simulations (Figure 4). However, the plateau does not respond homogeneously in terms of precipitation change as in the ensemble, which is also the case for the vertical pressure velocity (Figure A5 in Supporting Information S1 and Figure 8). The WRF simulations indicate a decrease in precipitation over southeast Anatolia and its extension

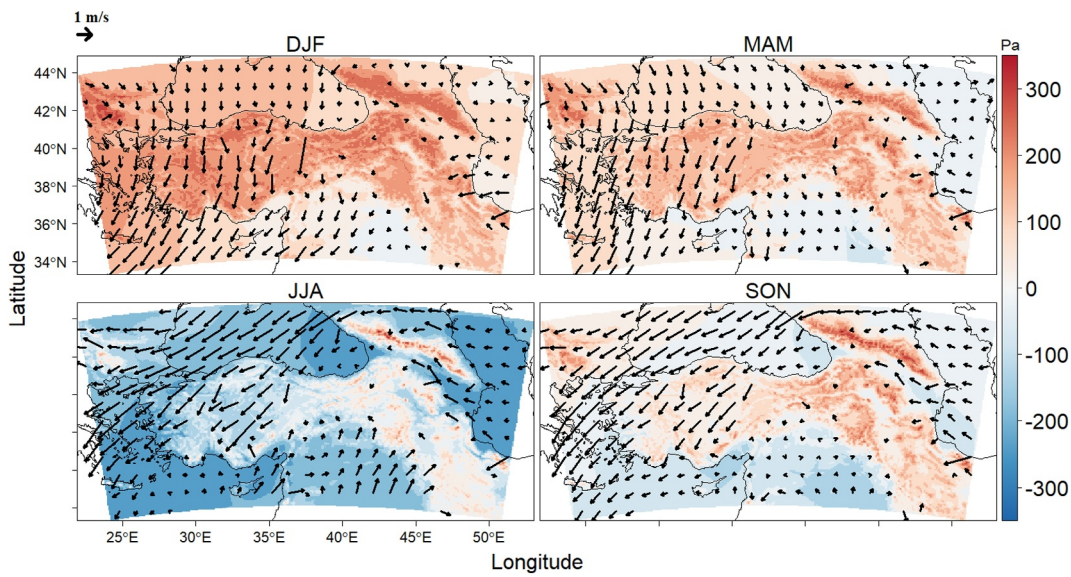

Figure 6. The low-level (850 hPa) circulation (winds as vectors) and SLP (shadings) change between 1995–2014 and the corresponding pseudo-future period for each season obtained from the WRF simulations for the EMBS domain. The wind vectors are in units of m/s, and SLP is in units of pascal. The reference vector is presented in the upper left.

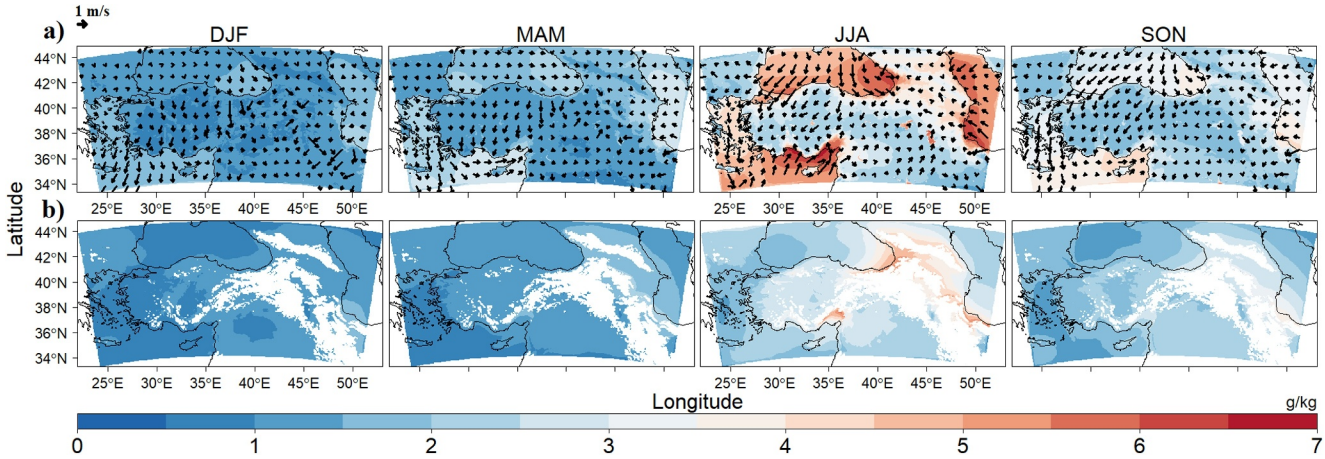

Figure 7. The specific humidity changes between 1995–2014 and the corresponding pseudo-future period for each season obtained from the WRF simulations for the EMBS domain. (a) The near-surface level (at 10 m for the winds and 2 m for the specific humidity) changes in specific humidity (shading) and wind patterns (vectors). (b) The low-level (850 hPa) changes in specific humidity. The wind vectors are in units of m/s, and specific humidity is in units of g/kg. The reference vector is presented in the upper left.

toward Syria and northern Iraq due to more pronounced mid-level tropospheric subsidence and high dew-point depression (Figure 9a). It shows that the "forced down" effect of the northerlies is limited along a belt, crossing mountain ranges over the southern EMBS. A similar phenomenon to the northern EMBS may explain the increase in precipitation over the southwest coasts of the Caspian Sea. Here, the wind patterns are easterly and perpendicular to the mountain range, resulting in an escalated upward movement of the moist air parcel. Besides, here is one of the rare regions (southwest coasts of the Caspian Sea and inner highlands) where the dew-point depression decreases (Figure 9a). It may also explain the increase in precipitation over the Greater Caucasus with the exception of its northwest margin, where the dew-point depression and mid-tropospheric subsidence increase, thus appearing to be responsible for the precipitation suppression. As for warming, the eastern Anatolian Plateau shows maxima at 8.8°C, which is about 2.4°C more than that in the GCM ensemble (Figure 9b and Figure

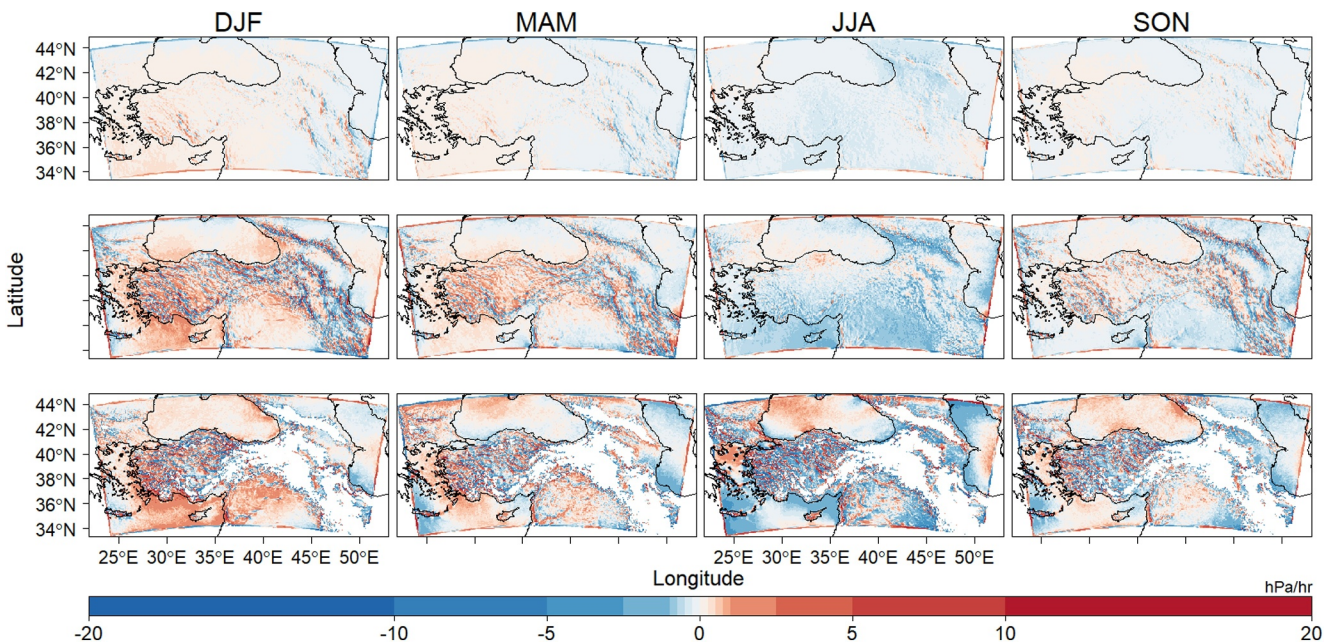

Figure 8. The vertical pressure velocity (omega) change between 1995–2014 and the corresponding pseudo-future period in the units of hPa/hr for each season obtained from the WRF simulations for the EMBS domain. The omega changes are presented in 200 hPa (in the top), 500 hPa (in the middle), and 850 hPa (in the bottom) pressure levels.

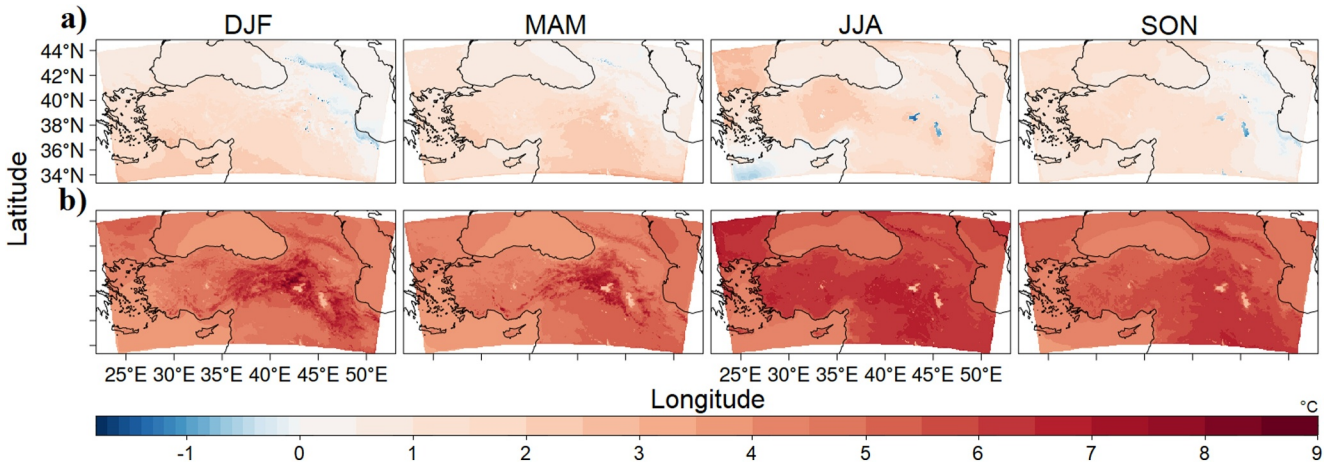

Figure 9. The dew-point depression (a) and near-surface temperature (b) changes between 1995–2014 and the corresponding pseudo-future period in the units of °C for each season obtained from the WRF simulations for the EMBS domain. The dew-point depression was averaged with the values between the near-surface and 700 hPa pressure level.

A6 in Supporting Information S1). The same region largely loses its winter snow cover (not shown) and experiences significant surface drying (Figure A7 in Supporting Information S1). Warming in the remaining regions is not below 2.2°C and warming over land is up to 2°C more than over the sea. It should be noted that global winter warming is around 4.1°C between 2081–2100 and 1995–2014 under the SSP5-8.5 scenario for a 34-model ensemble (hereafter IPCC SSP5-8.5 long-term) (Iturbide et al., 2022). The decrease of the land-sea temperature contrast in winter, pointed out by Tuel and Eltahir (2020), is further attenuated by high-resolution WRF simulation. This may also better explain the anticyclone development, hence the suppression of precipitation in the Mediterranean region.

The spring season shows a similar low-level circulation pattern as in winter but with a moister atmosphere (Figures 6 and 7). Although the anomalous ridge softens the blow, it still manifests itself over the diagonal corridor between the Aegean and Mediterranean Sea by almost all level subsidence (Figures 5, 6, and 8). It mostly explains precipitation decrease over the regions that fall into the corridor (Figure 4b). Similar to the winter season, near-surface warming shows its seasonal maxima over the eastern Anatolian Plateau and the high-altitude regions of the Taurus mountains with 8°C, which is about 2.3°C more than that in the GCM ensemble (Figure 9b and Figure A6 in Supporting Information S1). Near-surface warming is accompanied by drying over the same regions (Figure A7 in Supporting Information S1). The global spring warming is around 3.8°C for the IPCC SSP5-8.5 long-term.

During summer, the weakening of the subsidence by the heat-low formation over the eastern Mediterranean manifests over the EMBS, which translates to slight precipitation increases over the eastern Mediterranean Region and a corridor between the east of the Marmara Region and the west of the Mediterranean Region of Türkiye (Figures 4b, 5, 6, and 8). The precipitation increase is also prominent, with higher values over the eastern part of the Mediterranean Region of Türkiye, where humid air over its coasts ascends and is transported to the mountain range by low-level, perpendicular wind patterns. There are no significant precipitation changes by the WRF simulation over the Aegean Region and Aegean Sea as opposed to the GCM ensemble, which shows a slight but significant decrease in precipitation (Figure 4). It should be noted that Etesian winds strengthen over the Aegean Region and the Aegean Sea (Figure 7a). On the other hand, the low and mid-tropospheric subsidence are accompanied by a precipitation decrease over the northwestern EMBS, including northern Greece and Bulgaria (Figures 4b and 8). As for the southeastern EMBS, the convergent flow does not translate to a substantial precipitation increase over the southern Persian trough (Figures 4b and 6). A large discrepancy in summer precipitation is present over the northeastern EMBS centering the Greater Caucasus between the GCM ensemble and the WRF simulations. The WRF simulation shows an anomalous precipitation increase, while the GCM ensemble shows a substantial decrease (Figure 4). In fact, the low-level (850 hPa) circulation change draws a similar picture over the region (Figure 6). Besides, the low and upper-tropospheric (200 hPa) pressure movements have a similar pattern (Figure 8 and Figure A5 in Supporting Information S1). However, the vertical pressure velocity has an

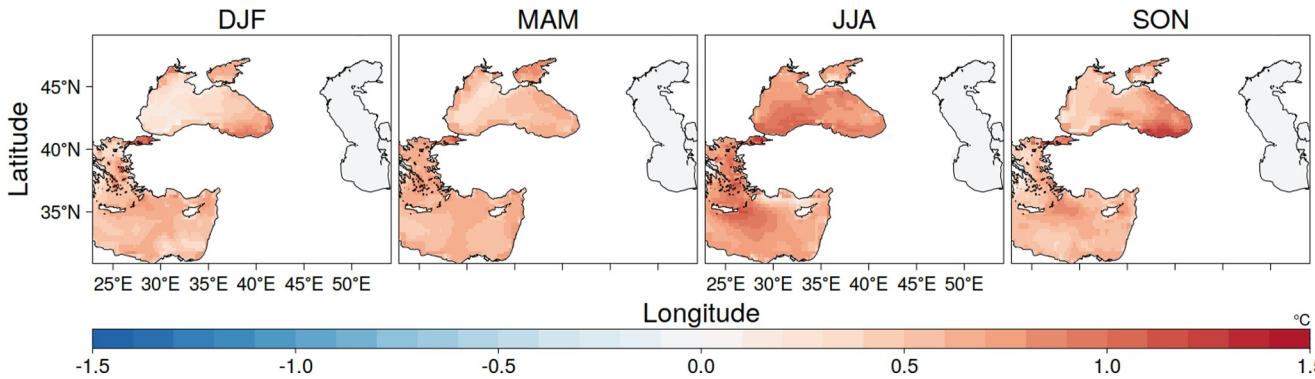

Figure 10. The seasonal mean warming differences between three GCMs (CMCC-CM2-SR5, CMCC-ESM2, HadGEM3-GC31-MM) SST and all available GCM ensemble SST (three GCMs SST increase minus full ensemble SST increase) between 2071–2100 (future SSP5-8.5 scenario) and 1985–2014 (historical) periods.

opposite sign in the mid-troposphere. The WRF simulation exhibits a strong air ascent, while the GCM ensemble shows a descent over the Greater Caucasus in the mid-troposphere. Moreover, the WRF simulations show a more specific humidity increase in near-surface and lower troposphere than the GCM ensemble with an extended area (Figure 7 and Figure A8 in Supporting Information S1). It should also be noted that the future decrease in SLP over the nearest coastal regions of the Greater Caucasus in summer with WRF simulations is significantly more than the GCM ensemble (up to 1 hPa more negative changes; Figure 6 and Figure A4 in Supporting Information S1). The following section investigates the main reason behind this discrepancy with additional analysis. The near-surface relative humidity increase is prominent over the coastal regions and inner lakes of the EMBS with WRF simulations (Figure A7 in Supporting Information S1). The near-surface temperature increase has a more homogenous appearance, where the GCM ensemble shows its seasonal maxima over northwestern EMBS with around 7.3 and around 7.2°C over western Anatolia (Figure A6 in Supporting Information S1). The WRF simulations agree for northwestern EMBS in terms of warming amount and expect 0.5°C less warming for western Anatolia. However, it shows warming maxima over the high altitudes of the Greater Caucasus with values exceeding 7.3°C (Figure 9b). The global summer warming is around 3.9°C in the IPCC SSP5-8.5 long-term.

The fall season demonstrates similar low-level circulation and precipitation patterns to those in summer over most of the EMBS (Figures 4 and 6). Compared to the summer season, a less intense but still strong precipitation increase signal exists over the Greater Caucasus and Türkiye's eastern Black Sea coast. It seems related to the attenuation of the mid-and upper-tropospheric ascent and lower increase of the specific humidity in the near-surface and lower troposphere as the circulation pattern is nearly unchanged. The near-surface warming also has a similar pattern between the GCM ensemble and the WRF simulation; however, the WRF simulations show that the high altitudes of the Greater Caucasus are one of the most warming regions, with warming exceeding 6.5°C. However, the region does not tend to be exposed to surface drying (Figure A7 in Supporting Information S1) due to the high precipitation in the summer and fall seasons (Figure 4). The global fall warming is around 4°C in the IPCC SSP5-8.5 long-term.

3.4. Impact of SST Availability in the GCM Ensemble

We want to emphasize the impact of the SST availability of the GCM ensemble members for the Caspian Sea to explain the most likely reason for the anomalous precipitation increase over the Greater Caucasus and nearby regions, especially in summer. Among the 13-member ensemble (Table 1), only CMCC-CM2-SR5, CMCC-ESM2, and HadGEM3-GC31-MM provide SST data for the Caspian Sea. Therefore, we were limited to using these three GCMs in the SST perturbation, which was updated in WRF simulations at a 6-hourly time step. The problem of SST availability is most likely causing more warming for the Caspian Sea since the three GCMs providing information for the Caspian Sea consistently produce warmer SST projections than the full ensemble over the Aegean and Mediterranean seas, besides the Black Sea (Figure 10). It can explain the strong increase in near-surface and lower tropospheric specific humidity in the WRF simulations in summer, as the specific humidity increase in the GCM ensemble is relatively weak (Figure 7 and Figure A8 in Supporting Information S1). It can also explain the ascending mid-tropospheric air and significantly more negative SLP over the nearest coastal regions of the Greater Caucasus in the WRF simulations. It is worth mentioning that fine-scale features (water and

energy exchanges) provided by WRF simulations may also help trigger the ascent. These factors can explain the anomalous precipitation increase over the Greater Caucasus and nearby regions since other primary governing factors, that is, large-scale low-level circulation, are well captured by the WRF simulations. Indeed, a high precipitation increase is also simulated for the fall season, where the low-level circulation has a similar pattern to that in summer. However, the increase in specific humidity in fall is weaker compared to summer, although Caspian Sea SSTs probably remain warmer than expected (Figure 10) (three GCMs SST increase minus full ensemble SST increase). In combination with the attenuation of the heat-low effect (Figure 8), this could explain a less intense but still obvious increase in precipitation in the fall season. On the other hand, during winter and spring, when the large-scale low-level circulation (anomalous ridge in the Mediterranean) does not directly affect those regions, the Greater Caucasus and nearby regions appear less SST-sensitive. Besides, the near-surface and lower troposphere specific humidity increases are in good agreement between the GCM ensemble (boundary) and WRF simulations for winter and spring (Figure 7 and Figure A8 in Supporting Information S1).

4. Discussion

There is a widespread consensus that the Mediterranean is one of the climate change hotspots featuring strong warming and drying trends as a result of increasing GHGs concentrations (Ali et al., 2022; Bağçaci et al., 2021; Barcikowska et al., 2018; Giorgi, 2006; Giorgi & Lionello, 2008; Tuel & Eltahir, 2020). While there is a high confidence for overall warming, drying signals are more regional. For example, IPCC AR6 (2021) expects precipitation to decrease over very few regions (Mediterranean, Southern Africa, southwestern Australia) (medium confidence) by mid-century (medium confidence). Hence, tendencies toward increased precipitation amounts can also be expected when considering climatic transitional zone features of the complex topography in the EMBS, as shown by the CMIP6 GCM ensemble. In this study, we can mainly confirm these findings by regional high-resolution simulations (4 km grid spacing) based on the PGW method with the WRF model for the end of the century (2071–2100). However, the WRF simulations provide some added value in comparison to the CMIP6 GCM ensemble. For instance, the GCM ensemble shows a more homogeneous maximum warming trend in summer in comparison to the more complex patterns in the downscaled simulations. The WRF simulations exhibit a detailed maxima of warming and drying over the northeastern Anatolian Plateau in winter and spring, which can be explained by a strong reduction in snow cover. This causes reduced snow-albedo feedback and leads to an increase in winter/spring temperatures. The region's crucial need for water availability is impacted by the reduction of snow cover in the future, which also has an impact on the timing of snowmelt runoff (Sen et al., 2011; Yucel et al., 2015). On the other hand, the future changes in winter and spring precipitation climatology are generally well captured with the WRF simulations. We clearly see the impact of the development of the intense anomalous ridge in the circulation and precipitation response. More northeasterlies and drying over the south and southwestern EMBS in winter are also possible outcomes of the more positive NAO phase and the weakening of the Mediterranean storm track. Tuel and Eltahir (2020) showed that the attenuation of land-sea temperature contrast and large-scale upper tropospheric flow changes have a comparable impact on the development of the anomalous ridge, resulting in the decline of winter precipitation over the Mediterranean. As we did not conduct any component analysis in this study, we cannot state which effect is more substantial. Nevertheless, we can confirm the attenuation of the land-sea temperature contrast, which may contribute to an anticyclonic environment over the Mediterranean and Aegean coasts. However, our WRF simulations did not show precipitation decrease over the easternmost coasts of the Black Sea and near inland regions in winter; instead, they showed an increase in line with the GCM ensemble, which means land-sea temperature contrast attenuation cannot offset other factors and is incapable of precipitation suppression over the region.

Barcikowska et al. (2020) identify a weakening of the subsidence over the eastern Mediterranean and a strengthening over the central Mediterranean in future projections for summer. They showed that these changes amplify the SLP dipole differences, resulting in stronger Etesian winds. Here, we confirm the tendency to the heat-low formation over the eastern Mediterranean, although it is more to the west than the authors indicated. However, we did not observe a SLP increase in the GCM ensemble over the central Mediterranean (Figure 5). It causes the 850 hPa wind pattern to shift from a northerly to a northeasterly direction along the Aegean Sea, although the Etesians strengthen by maintaining their direction at near surface level (Figure 7a). A similar opposite sign of SLP exists over the Black Sea. Here, we observed a negative SLP change over the Black Sea, where the low-level wind blows from the Caspian Sea towards the Black Sea, in an agreement between the GCM ensemble and the WRF, although in different quantities (Figure 6 and Figure A4 in Supporting Information S1).

Contrary to Barcikowska et al. (2020), albeit a direct comparison may not be outrightly fair since they compared the 300 warmest and 300 coolest summers (July), we did not observe mid-tropospheric subsidence development over northeastern Anatolia and the Greater Caucasus as a result of the surface warming (Figures 8 and 9b). The heat-low effect in the summer season allows air to ascent over the EMBS more to the extent that it weakens the subsidence in the troposphere. This is one of the main factors explaining the slight increase in precipitation over the eastern Mediterranean Region and a corridor between the east of the Marmara Region and the west of the Mediterranean Region of Türkiye, as other factors, such as increased dew-point temperature and land-sea temperature contrast in the summer season (Figures 8 and 9a), favor suppressed precipitation. In summer as opposed to winter, an increase in the land-sea temperature contrast may suppress relative humidity and, thus, precipitation increase over the Mediterranean coasts by increasing water holding capacity over land more than over the sea (Barcikowska et al., 2020; Rowell & Jones, 2006). For the fall season, a reduction of precipitation over the Mediterranean and Aegean coastlines of Türkiye is associated with the diminishing heat-low effect formed in summer. There has been no strong increase in precipitation in the region situated in the southern Persian trough, which can be attributed to the dry air transported from the Arabian Desert. The opposite trend in precipitation in the northwestern EMBS, namely a decrease in summer and an increase during autumn, is the result of variances in subsidence in the low and mid-troposphere and the alteration in wind patterns relative to the mountain range. Additionally, there is an increment of almost 1°C in dewpoint depression during the summer season compared to the fall season. The reduction in summer precipitation over the northernmost Black Sea coast of Türkiye is stronger compared to autumn, which appears to be connected to the weakening of the mid-tropospheric subsidence. The remaining regions, except for northeastern EMBS, exhibit the same precipitation features for the two seasons.

The anomalous precipitation increase, particularly during summer over the Greater Caucasus and nearby areas, prompted us to conduct further investigations. We started with an investigation into the excessive moisture source in the near-surface and lower troposphere, which was found to be the source of the anomalous increase in precipitation. This increase cannot be attributed to the GCM boundary conditions, as the increase in specific humidity for the future is weak in the GCM ensemble, and the WRF simulations accurately captured the large-scale low-level circulation. Thus, we have investigated the SST increases in the future, where any anomaly could result in additional moisture being generated in the WRF simulations. We have shown that only three GCMs among 13 have SST information for the Caspian Sea, where those three consistently exhibit warmer temperatures than the entire ensemble for the Black, Aegean, and Mediterranean seas. Based on this, we hypothesized that there may be a similar SST overestimation for the Caspian Sea, potentially explaining the excessive moisture resulting in an anomalous precipitation increase. The warmer-than-expected Caspian Sea could also potentially account for the ascending air in the mid-troposphere, facilitating an increase in precipitation by extending the heat-low effect. A recent study by Xue et al. (2023) showed that SLP perturbation in a PGW study may cause a significant alteration in the warming signal coming from GCMs. They stated that more SLP increases almost halved the warming signal over the ocean and justified the fact by the hypsometric equation, that is, an increase in the SLP must be compensated by a decrease in warming and vice versa. Our WRF simulations generally preserve warming signals over the seas; however, the warmer-than-expected Caspian Sea may explain significantly more negative SLP differences over the nearest coast of the Greater Caucasus, another factor behind the anomalous precipitation increase over the Greater Caucasus and nearby regions. On the other hand, Barcikowska et al. (2020) demonstrated a strong precipitation increase during summer over the highlands of the Greater Caucasus (in their Figure 7), which is consistent with our WRF simulations. This confirmation enhances our assurance, particularly over the high-altitude regions of the Greater Caucasus, where there is a robust increase in precipitation. It should be noted that modeling precipitation is challenging as it is highly dependent on chaotic, moist atmospheric processes and complex triggering dynamics. As high-resolution simulations require shorter integration time steps, it is more challenging to model the location and timing of precipitation events precisely when considering their variability and spectral power (Tapiador et al., 2019). Hence, balancing the need for a finer resolution to capture small-scale features with computational efficiency poses a persistent challenge in precipitation modeling.

5. Conclusion

In this study, we provided an outlook of future climatic changes in the EMBS region based on dynamic downscaling of the state-of-the-art CMIP6 GCM ensemble with the WRF model in the context of the PGW approach. We focused on climate changes for the end of the century (2071–2100) by the SSP5-8.5 scenario. The findings indicate a general agreement with the literature regarding future warming, drying/wetting tendencies and

circulation changes. The added value of the very high-resolution simulations becomes apparent, particularly over regions with complex topography and different climatic transitional features. Some regions at risk of adverse effects in future winter seasons include the Aegean and Mediterranean coasts and the inner highlands of the EMBS, where a significant decrease in precipitation is expected. On the contrary, Türkiye's eastern Black Sea coasts and inner highlands, receiving high precipitation in today's climate conditions, are expected to face even more rainfall in the future, potentially leading to a greater frequency and severity of flood events. On the other hand, the summer season precipitation projections, among others, have high uncertainties related to SST availability, albeit large-scale low-level circulations and lower and upper tropospheric air movements are well captured by the regional WRF simulations. Owing to the limited number of GCMs that provide SSTs for the Caspian Sea, which probably faces a warm bias, our simulations indicate an anomalous future precipitation increase over the Greater Caucasus and nearby regions during summer. The dynamical downscaling of GCMs with comprehensive Caspian Sea data should be performed to examine further the rise in specific humidity and mid-tropospheric subsidence over these regions.

Conflict of Interest

The authors declare no conflicts of interest relevant to this study.

Data Availability Statement

The ground observations of precipitation and temperature for the territory of Türkiye were retrieved from Türkiye's General Directorate of Meteorology (GDM). The ground observations of temperature outside of Türkiye were retrieved from the World Meteorological Organization (WMO). The Global Precipitation Climatology Centre (GPCC, Schneider et al., 2022) monthly precipitation data set at 0.25° resolution, HOAPS/GPCC (Schröder et al., 2019) global daily precipitation data record at 0.5° resolution, EOBS (Cornes et al., 2018) daily precipitation and the near-surface temperature product at 0.1° resolution, and the Climate Research Unit at the University of East Anglia (CRU version 3.22, 1901–2013; Harris et al. (2014)) monthly near-surface temperature product at 0.5° resolution were utilized. The ERA5 reanalysis data set (Hersbach et al., 2020) can be obtained via https://cds.climate.copernicus.eu/ and CMIP6 (Eyring et al., 2016) historical and Shared Socioeconomic Pathways (SSPs) (O'Neill et al., 2016) data sets can be obtained via https://esgf-data.dkrz.de/projects/cmip6-dkrz/. The WRF model (Skamarock et al., 2021) can be downloaded via https://www2.mmm.ucar.edu/wrf/users/download/get_source.html. The simulations will be archived at TRUBA (Turkish High Computing Center) for a limited time and are available from the corresponding author upon request.

Acknowledgments

We would like to give special thanks to the Turkish High Performance and Grid Computing Center (TÜBİTAK ULAKBİM) and its referred National e-Science e-Infrastructure (TRUBA) unit in collaboration with the EURO-CC project. Their support was invaluable in terms of not only providing us national HPC facilities and funding open access for this paper but also helping us when running into a problem. We would like to express our sincere thanks to the two anonymous reviewers whose insightful comments and constructive feedback greatly contributed to the improvement of this article. The authors also would like to thank the World Climate Research Programme and its Working Group on Coupled Modeling, coordinated and promoted CMIP6. The authors also thank the climate modeling groups for producing and making publicly available their model outputs, the Earth System Grid Federation (ESGF) for archiving the data and providing access, and the multiple funding agencies who support CMIP6 and ESGF. Finally, the authors are grateful to the Turkish General Directorate of Meteorology for providing access to daily/monthly temperature and precipitation data throughout the country and the World Meteorological Organization for the daily/monthly near-surface temperature data outside Türkiye. The authors have no relevant financial or non-financial interests to disclose.

References

Ahmed, K., Sachindra, D. A., Shahid, S., Demirel, M. C., & Chung, E. S. (2019). Selection of multi-model ensemble of general circulation models for the simulation of precipitation and maximum and minimum temperature based on spatial assessment metrics. *Hydrology and Earth System Sciences*, *23*(11), 4803–4824. https://doi.org/10.5194/hess-23-4803-2019

Ali, E., Cramer, W., Carnicer, J., et al. (2022). Cross-chapter paper 4: Mediterranean region in: Climate change 2022. In H.-O. Pörtner, D. C. Roberts, M. Tignor, E. S. Poloczanska, K. Mintenbeck, A. Alegría, et al. (Eds.), *Impacts, adaptation and vulnerability. Contribution of working group II to the sixth assessment report of the intergovernmental panel on climate change*, *IPCC*. https://doi.org/10.1017/9781009325844

Alpert, P., Baldi, M., Ilani, R., Krichak, S., Price, C., Rodó, X., et al. (2006). Chapter 2 relations between climate variability in the Mediterranean region and the tropics: ENSO, South Asian and African monsoons, hurricanes and Saharan dust. *Developments in Earth and Environmental Sciences*, *4*, 149–177. https://doi.org/10.1016/S1571-9197(06)80005-4

Anagnostopoulou, C., Zanis, P., Katragkou, E., Tegoulias, I., & Tolika, K. (2014). Recent past and future patterns of the Etesian winds based on regional scale climate model simulations. *Climate Dynamics*, *42*(7–8), 1819–1836. https://doi.org/10.1007/s00382-013-1936-0

Bağçacı, S. Ç. (2023). *The analysis of current and future climate projections of Türkiye and the large-scale Eastern Mediterranean Black Sea region in the coarse and high resolutions*. Middle East Technical University.

Bağçaci, S. Ç., Yucel, I., Duzenli, E., & Yilmaz, M. T. (2021). Intercomparison of the expected change in the temperature and the precipitation retrieved from CMIP6 and CMIP5 climate projections: A Mediterranean hot spot case, Turkey. *Atmospheric Research*, *256*, 105576. https://doi.org/10.1016/j.atmosres.2021.105576

Barcikowska, M. J., Kapnick, S. B., & Feser, F. (2018). Impact of large-scale circulation changes in the North Atlantic sector on the current and future Mediterranean winter hydroclimate. *Climate Dynamics*, *50*(5–6), 2039–2059. https://doi.org/10.1007/s00382-017-3735-5

Barcikowska, M. J., Kapnick, S. B., Krishnamurty, L., Russo, S., Cherchi, A., & Folland, C. K. (2020). Changes in the future summer Mediterranean climate: Contribution of teleconnections and local factors. *Earth System Dynamics*, *11*(1), 161–181. https://doi.org/10.5194/esd-11-161-2020

Bozkurt, D., & Sen, O. L. (2013). Climate change impacts in the Euphrates-Tigris Basin based on different model and scenario simulations. *Journal of Hydrology*, *480*, 149–161. https://doi.org/10.1016/j.jhydrol.2012.12.021

Catto, J. L., Ackerley, D., Booth, J. F., Champion, A. J., Colle, B. A., Pfahl, S., et al. (2019). The future of midlatitude cyclones. *Current Climate Change Reports*, *5*(4), 407–420. https://doi.org/10.1007/s40641-019-00149-4

Chen, F., & Dudhia, J. (2001). Coupling and advanced land surface-hydrology model with the Penn State-NCAR MM5 modeling system. Part I: Model implementation and sensitivity. *Monthly Weather Review*, *129*(4), 569–585. https://doi.org/10.1175/1520-0493(2001)129<0569:CAALSH>2.0.CO;2

Cornes, R. C., van der Schrier, G., van den Besselaar, E. J. M., & Jones, P. D. (2018). An ensemble version of the E-OBS temperature and precipitation data sets [Dataset]. *Journal of Geophysical Research: Atmospheres*, *123*(17), 9391–9409. https://doi.org/10.1029/2017JD028200

Dutheil, C., Menkes, C., Lengaigne, M., Vialard, J., Peltier, A., Bador, M., & Petit, X. (2020). Fine-scale rainfall over New Caledonia under climate change. *Climate Dynamics*, *56*(1–2), 87–108. https://doi.org/10.1007/s00382-020-05467-0

Duzenli, E., Tabari, H., Willems, P., & Yilmaz, M. T. (2018). Decadal variability analysis of extreme precipitation in Turkey and its relationship with teleconnection patterns. *Hydrological Processes*, *32*(23), 3513–3528. https://doi.org/10.1002/hyp.13275

ECMWF. (2020). E-OBS daily gridded meteorological data for Europe from 1950 to present derived from in-situ observations [Dataset]. https://doi.org/10.24381/cds.151d3ec6

Eshel, G., & Farrell, B. F. (2000). Mechanisms of eastern Mediterranean rainfall variability. *Journal of the Atmospheric Sciences*, *57*(19), 3219–3232. https://doi.org/10.1175/1520-0469(2000)057<3219:MOEMRV>2.0.CO;2

Eyring, V., Bony, S., Meehl, G. A., Senior, C. A., Stevens, B., Stouffer, R. J., & Taylor, K. E. (2016). Overview of the coupled model intercomparison project phase 6 (CMIP6) experimental design and organization [Dataset]. *Geoscientific Model Development*, *9*(5), 1937–1958. https://doi.org/10.5194/gmd-9-1937-2016

Fujihara, Y., Tanaka, K., Watanabe, T., Nagano, T., & Kojiri, T. (2008). Assessing the impacts of climate change on the water resources of the Seyhan River Basin in Turkey: Use of dynamically downscaled data for hydrologic simulations. *Journal of Hydrology*, *353*(1–2), 33–48. https://doi.org/10.1016/j.jhydrol.2008.01.024

Giorgi, F. (2006). Climate change hot-spots. *Geophysical Research Letters*, *33*(8), L08707. https://doi.org/10.1029/2006GL025734

Giorgi, F., & Lionello, P. (2008). Climate change projections for the Mediterranean region. *Global and Planetary Change*, *63*(2–3), 90–104. https://doi.org/10.1016/j.gloplacha.2007.09.005

Gómez, B., & Miguez-Macho, G. (2017). The impact of wave number selection and spin-up time in spectral nudging. *Quarterly Journal of the Royal Meteorological Society*, *143*(705), 1772–1786. https://doi.org/10.1002/qj.3032

Harris, I., Jones, P. D., Osborn, T. J., & Lister, D. H. (2014). CRU TS3.22: Climatic research unit (CRU) time-series (TS) version 3.22 of high resolution gridded data of month-by-month variation in climate (Jan. 1901- Dec. 2013) [Dataset]. *NCAS British Atmospheric Data Centre*, *23*. https://doi.org/10.5285/18BE23F8-D252-482D-8AF9-5D6A2D40990C

Hersbach, H., Bell, B., Berrisford, P., Hirahara, S., Horányi, A., Muñoz-Sabater, J., et al. (2020). The ERA5 global reanalysis [Dataset]. *Quarterly Journal of the Royal Meteorological Society*, *146*(730), 1999–2049. https://doi.org/10.1002/qj.3803

Hong, S. Y., Noh, Y., & Dudhia, J. (2006). A new vertical diffusion package with an explicit treatment of entrainment processes. *Monthly Weather Review*, *134*(9), 2318–2341. https://doi.org/10.1175/MWR3199.1

Huang, Z., Zhong, L., Ma, Y., & Fu, Y. (2021). Development and evaluation of spectral nudging strategy for the simulation of summer precipitation over the Tibetan Plateau using WRF (v4.0). *Geoscientific Model Development*, *14*(5), 2827–2841. https://doi.org/10.5194/gmd-14-2827-2021

Hunt, K. M. R., Turner, A. G., & Shaffrey, L. C. (2020). The impacts of climate change on the winter water cycle of the western Himalaya. *Climate Dynamics*, *55*(7–8), 2287–2307. https://doi.org/10.1007/s00382-020-05383-3

Iacono, M. J., Delamere, J. S., Mlawer, E. J., Shephard, M. W., Clough, S. A., & Collins, W. D. (2008). Radiative forcing by long-lived greenhouse gases: Calculations with the AER radiative transfer models. *Journal of Geophysical Research*, *113*(D13), D13103. https://doi.org/10.1029/2008JD009944

Ikeda, K., Rasmussen, R., Liu, C., Newman, A., Chen, F., Barlage, M., et al. (2021). Snowfall and snowpack in the Western U.S. as captured by convection permitting climate simulations: Current climate and pseudo global warming future climate. *Climate Dynamics*, *57*(7–8), 2191–2215. https://doi.org/10.1007/s00382-021-05805-w

IPCC AR6. (2021). Climate change 2021 – The physical science basis. In V. Masson-Delmotte, P. Zhai, A. Pirani, S. L. Connors, C. Péan, S. Berger, et al. (Eds.), *Contribution of working group I to the sixth assessment report of the intergovernmental panel on climate change*. Cambridge University Press. In press. https://doi.org/10.1017/9781009157896

Iturbide, M., Fernández, J., Gutiérrez, J. M., Pirani, A., Huard, D., Al Khourdajie, A., et al. (2022). Implementation of FAIR principles in the IPCC: The WGI AR6 Atlas repository [Dataset]. *Scientific Data*, *9*(1), 629. https://doi.org/10.1038/s41597-022-01739-y

Kadioğlu, M., Tulunay, Y., & Borhan, Y. (1999). Variability of Turkish precipitation compared to El Nino events. *Geophysical Research Letters*, *26*(11), 1597–1600. https://doi.org/10.1029/1999GL900305

Kim, J., Ivanov, V. Y., & Fatichi, S. (2016). Climate change and uncertainty assessment over a hydroclimatic transect of Michigan. *Stochastic Environmental Research and Risk Assessment*, *30*(3), 923–944. https://doi.org/10.1007/s00477-015-1097-2

Kutiel, H., & Benaroch, Y. (2002). North Sea-Caspian pattern (NCP)—An upper level atmospheric teleconnection affecting the Eastern Mediterranean: Identification and definition. *Theoretical and Applied Climatology*, *71*(1–2), 17–28. https://doi.org/10.1007/s704-002-8205-x

Li, Y., Li, Z., Zhang, Z., Chen, L., Kurkute, S., Scaff, L., & Pan, X. (2019). High-resolution regional climate modeling and projection over western Canada using a weather research forecasting model with a pseudo-global warming approach. *Hydrology and Earth System Sciences*, *23*(11), 4635–4659. https://doi.org/10.5194/hess-23-4635-2019

Lionello, P., Bhend, J., Buzzi, A., Della-Marta, P., Krichak, S., Jansà, A., et al. (2006). Chapter 6 cyclones in the Mediterranean region: Climatology and effects on the environment. *Developments in Earth and Environmental Sciences*, *4*, 325–372. https://doi.org/10.1016/S1571-9197(06)80009-1

Liu, C., Ikeda, K., Rasmussen, R., Barlage, M., Newman, A. J., Prein, A. F., et al. (2017). Continental-scale convection-permitting modeling of the current and future climate of North America. *Climate Dynamics*, *49*(1–2), 71–95. https://doi.org/10.1007/s00382-016-3327-9

Mastrantonas, N., Herrera-Lormendez, P., Magnusson, L., Pappenberger, F., & Matschullat, J. (2021). Extreme precipitation events in the Mediterranean: Spatiotemporal characteristics and connection to large-scale atmospheric flow patterns. *International Journal of Climatology*, *41*(4), 2710–2728. https://doi.org/10.1002/joc.6985

Miguez-Macho, G., Stenchikov, G. L., & Robock, A. (2004). Spectral nudging to eliminate the effects of domain position and geometry in regional climate model simulations. *Journal of Geophysical Research*, *109*(D13), D13104. https://doi.org/10.1029/2003JD004495

Miguez-Macho, G., Stenchikov, G. L., & Robock, A. (2005). Regional climate simulations over North America: Interaction of local processes with improved large-scale flow. *Journal of Climate*, *18*(8), 1227–1246. https://doi.org/10.1175/JCLI3369.1

O'Neill, B. C., Tebaldi, C., Van Vuuren, D. P., Eyring, V., Friedlingstein, P., Hurtt, G., et al. (2016). The scenario model intercomparison project (ScenarioMIP) for CMIP6 [Dataset]. *Geoscientific Model Development*, *9*, 3461–3482. https://doi.org/10.5194/gmd-9-3461-2016

Önol, B. (2012). Effects of coastal topography on climate: High-resolution simulation with a regional climate model. *Climate Research*, *52*, 159–174. https://doi.org/10.3354/cr01077

Önol, B., Bozkurt, D., Turuncoglu, U. U., Sen, O. L., & Dalfes, H. N. (2014). Evaluation of the twenty-first century RCM simulations driven by multiple GCMs over the eastern Mediterranean-Black Sea region. *Climate Dynamics*, *42*(7–8), 1949–1965. https://doi.org/10.1007/s00382-013-1966-7

Poupkou, A., Zanis, P., Nastos, P., Papanastasiou, D., Melas, D., Tourpali, K., & Zerefos, C. (2011). Present climate trend analysis of the Etesian winds in the Aegean Sea. *Theoretical and Applied Climatology*, *106*(3–4), 459–472. https://doi.org/10.1007/s00704-011-0443-7

Rodwell, M. J., & Hoskins, B. J. (1996). Monsoons and the dynamics of deserts. *Quarterly Journal of the Royal Meteorological Society*, *122*(534), 1385–1404. https://doi.org/10.1256/smsqj.53407

Rodwell, M. J., & Hoskins, B. J. (2001). Subtropical anticyclones and summer monsoons. *Journal of Climate*, *14*(15), 3192–3211. https://doi.org/10.1175/1520-0442(2001)014<3192:SAASM>2.0.CO;2

Rowell, D. P., & Jones, R. G. (2006). Causes and uncertainty of future summer drying over Europe. *Climate Dynamics*, *27*(2–3), 281–299. https://doi.org/10.1007/s00382-006-0125-9

Schär, C., Frei, C., Lüthi, D., & Davies, H. C. (1996). Surrogate climate-change scenarios for regional climate models. *Geophysical Research Letters*, *23*(6), 669–672. https://doi.org/10.1029/96GL00265

Schneider, U., Hänsel, S., Finger, P., Rustemeier, E., & Ziese, M. (2022). GPCC full data monthly product version 2022 at 0.25°: Monthly land-surface precipitation from rain-gauges built on GTS-based and historical data [Dataset]. *Global Precipitation Climatology Centre*. https://doi.org/10.5676/DWD_GPCC/FD_M_V2022_025

Schröder, M., Becker, A., Dietzsch, F., Fennig, K., Graw, K., Gutenstein, M., et al. (2019). HOAPS/GPCC global daily precipitation data record with uncertainty estimates using satellite and gauge based observations (at 1.0° and 2.5°, at 0.5° only Europe) [Dataset]. *Global Precipitation Climatology Centre*. https://doi.org/10.5676/DWD_CDC/HOGP_050/V002

Sen, O. L., Ezber, Y., & Bozkurt, D. (2019). Euro-Mediterranean climate variability in boreal winter: A potential role of the East Asian trough. *Climate Dynamics*, *52*(11), 7071–7084. https://doi.org/10.1007/s00382-018-4573-9

Şen, Ö. L., Göktürk, O. M., & Bozkurt, D. (2015). Changing climate: A great challenge for Turkey. *Journal of the Black Sea/Mediterranean Environment*, *21*, 97–104.

Sen, O. L., Unal, A., Bozkurt, D., & Kindap, T. (2011). Temporal changes in the Euphrates and Tigris discharges and teleconnections. *Environmental Research Letters*, *6*(2), 024012. https://doi.org/10.1088/1748-9326/6/2/024012

Simpson, I. R., Seager, R., Shaw, T. A., & Ting, M. (2015). Mediterranean summer climate and the importance of middle east topography. *Journal of Climate*, *28*(5), 1977–1996. https://doi.org/10.1175/JCLI-D-14-00298.1

Skamarock, W. C., Klemp, J. B., Dudhia, J., Gill, D. O., Liu, Z., Berner, J., et al. (2021). A description of the advanced research WRF model version 4.3 [Software]. https://doi.org/10.5065/1dfh-6p97

Tapiador, F. J., Roca, R., Del Genio, A., Dewitte, B., Petersen, W., & Zhang, F. (2019). Is precipitation a good metric for model performance? *Bulletin of the American Meteorological Society*, *100*(2), 223–233. https://doi.org/10.1175/BAMS-D-17-0218.1

Thompson, G., Field, P. R., Rasmussen, R. M., & Hall, W. D. (2008). Explicit forecasts of winter precipitation using an improved bulk microphysics scheme. Part II: Implementation of a new snow parameterization. *Monthly Weather Review*, *136*(12), 5095–5115. https://doi.org/10.1175/2008MWR2387.1

Tiedtke, M. (1989). A comprehensive mass flux scheme for cumulus parameterization in large-scale models. *Monthly Weather Review*, *117*(8), 1779–1800. https://doi.org/10.1175/1520-0493(1989)117<1779:ACMFSF>2.0.CO;2

Trigo, I. F., Bigg, G. R., & Davies, T. D. (2002). Climatology of cyclogenesis mechanisms in the Mediterranean. *Monthly Weather Review*, *130*(3), 549–569. https://doi.org/10.1175/1520-0493(2002)130<0549:COCMIT>2.0.CO;2

Trigo, R., Xoplaki, E., Zorita, E., Luterbacher, J., Krichak, S. O., Alpert, P., et al. (2006). Chapter 3 relations between variability in the Mediterranean region and mid-latitude variability. *Developments in Earth and Environmental Sciences*, *4*, 179–226. https://doi.org/10.1016/S1571-9197(06)80006-6

Tuel, A., & Eltahir, E. A. B. (2020). Why is the Mediterranean a climate change hot spot? *Journal of Climate*, *33*(14), 5829–5843. https://doi.org/10.1175/JCLI-D-19-0910.1

Türkeş, M., & Erlat, E. (2006). Influences of the North Atlantic oscillation on precipitation variability and changes in Turkey. *Nuovo Cimento-Societa Italiana di Fisica Sezione C*. https://doi.org/10.1393/ncc/i2005-10228-8

Tyrlis, E., & Lelieveld, J. (2013). Climatology and dynamics of the summer Etesian winds over the eastern Mediterranean. *Journal of the Atmospheric Sciences*, *70*(11), 3374–3396. https://doi.org/10.1175/JAS-D-13-035.1

Van Garderen, L., Feser, F., & Shepherd, T. G. (2021). A methodology for attributing the role of climate change in extreme events: A global spectrally nudged storyline. *Natural Hazards and Earth System Sciences*, *21*(1), 171–186. https://doi.org/10.5194/nhess-21-171-2021

Von Storch, H., Langenberg, H., & Feser, F. (2000). A spectral nudging technique for dynamical downscaling purposes. *Monthly Weather Review*, *128*(10), 3664–3673. https://doi.org/10.1175/1520-0493(2000)128<3664:ASNTFD>2.0.CO;2

Waldron, K. M., Paegle, J., & Horel, J. D. (1996). Sensitivity of a spectrally filtered and nudged limited-area model to outer model options. *Monthly Weather Review*, *124*(3), 529–547. https://doi.org/10.1175/1520-0493(1996)124<0529:SOASFA>2.0.CO;2

Wang, J., & Kotamarthi, V. R. (2013). Assessment of dynamical downscaling in near-surface fields with different spectral nudging approaches using the nested regional climate model (NRCM). *Journal of Applied Meteorology and Climatology*, *52*(7), 1576–1591. https://doi.org/10.1175/JAMC-D-12-0302.1

Xoplaki, E. (2002). *Climate variability over the Mediterranean*. University of Bern.

Xoplaki, E., González-Rouco, J. F., Luterbacher, J., & Wanner, H. (2004). Wet season Mediterranean precipitation variability: Influence of large-scale dynamics and trends. *Climate Dynamics*, *23*(1), 63–78. https://doi.org/10.1007/s00382-004-0422-0

Xue, Z., Ullrich, P., & Leung, L. Y. R. (2023). Sensitivity of the pseudo-global warming method under flood conditions: A case study from the northeastern US. *Hydrology and Earth System Sciences*, *27*(9), 1909–1927. https://doi.org/10.5194/hess-27-1909-2023

Yucel, I., Güventürk, A., & Sen, O. L. (2015). Climate change impacts on snowmelt runoff for mountainous transboundary basins in eastern Turkey. *International Journal of Climatology*, *35*(2), 215–228. https://doi.org/10.1002/joc.3974

Zappa, G., & Shepherd, T. G. (2017). Storylines of atmospheric circulation change for European regional climate impact assessment. *Journal of Climate*, *30*(16), 6561–6577. https://doi.org/10.1175/JCLI-D-16-0807.1

Zhang, C., Wang, Y., & Hamilton, K. (2011). Improved representation of boundary layer clouds over the southeast Pacific in ARW-WRF using a modified Tiedtke cumulus parameterization scheme. *Monthly Weather Review*, *139*(11), 3489–3513. https://doi.org/10.1175/MWR-D-10-05091.1

Zhang, C., Wang, Y., Hamilton, K., & Lauer, A. (2016). Dynamical downscaling of the climate for the Hawaiian Islands. Part II: Projection for the late twenty-first century. *Journal of Climate*, *29*(23), 8333–8354. https://doi.org/10.1175/JCLI-D-16-0038.1

Ziv, B., Saaroni, H., & Alpert, P. (2004). The factors governing the summer regime of the eastern Mediterranean. *International Journal of Climatology*, *24*(14), 1859–1871. https://doi.org/10.1002/joc.1113